Turbulent flow in a square duct with strong curvature

By J. A. C. HUMPHREY,

Department of Mechanical Engineering, University of California,
Berkeley, California

J. H. WHITELAW

Department of Mechanical Engineering, Fluids Section, Imperial College, London

AND G. YEE

Science Applications Incorporated, San Leandro, California

The steady, incompressible, isothermal, developing flow in a square-section curved duct with smooth walls has been investigated. The 40×40 mm duct had a radius ratio of 2·3 with long upstream and downstream straight ducts attached. Measurements of the longitudinal and radial components of mean velocity, and corresponding components of the Reynolds-stress tensor, were obtained with a laser-Doppler anemometer at a Reynolds number of 4×10^4 and in various cross-stream planes. The secondary mean velocities, driven mainly by the pressure field, attain values up to 28 % of the bulk velocity and are largely responsible for the convection of Reynolds stresses in the cross-stream plane. Production of turbulent kinetic energy predominates close to the outer-radius wall and regions with negative contributions to the production exist. Thus, at a bend angle of 90° and near the inner-radius wall, $\overline{u_\theta u_r}\, \partial U_\theta / \partial r$ is positive and represents a negative contribution to the generation of turbulent kinetic energy.

In spite of the complex mean flow and Reynolds stress distributions, the cross-stream flow is controlled mainly by the centrifugal force, radial pressure gradient imbalance. As a consequence, calculated mean velocity results obtained from the solution of elliptic differential equations in finite difference form and incorporating a two-equation turbulence model are not strongly dependent on the model; numerical errors are of greater importance.

1. Introduction

Flow in a curved duct is characterized by a stress field with stabilizing effects near to the inner-radius wall and destabilizing effects close to the outer radius wall. These effects, and the related turbulence features, have been considered by Bradshaw (1973) for two-dimensional, boundary-layer type flows but as indicated by Johnston (1976), little work has been directed to confined curved-duct flow. This lack of information exists in spite of the relevance of confined curved flows to bends, headers, alternator cooling ducts and the blade passages of compressors and turbines. A review of engineering design information of relevance to bends has been provided by Ward-Smith (1971) but does not offer substantial contributions to the understanding of flow

mechanisms. More recently Mori *et al.* (1971) and Pratap & Spalding (1975) have made experimental contributions but, in common with many previous investigations of three-dimensional curved-duct flows, these are limited mainly to Pitot-tube measurements and, therefore, substantially to the determination of longitudinal mean velocity. Pierce & Duerson (1975) using hot-wire anemometry techniques have measured components of the Reynolds-stress tensor in an end wall three-dimensional channel boundary layer but these are of limited extent.

A major reason for the lack of detailed information of curved-duct flow stems from measurement difficulties which have been partly removed by the development of laser-Doppler anemometry. Humphrey, Taylor & Whitelaw (1977), in a previous investigation of a laminar flow in the present bend, made use of a laser-Doppler anemometer to measure the longitudinal component of mean velocity. This study followed an earlier investigation of developing turbulent flow in a square duct by Melling & Whitelaw (1976) and provides the basis for the precise measurement of two components of mean velocity and the corresponding normal and Reynolds stresses in the same rectangular curved duct at a Reynolds number corresponding to turbulent flow.

Significant contributions to the understanding of curved-duct flows have been made through the solution of reduced forms of the Navier–Stokes equations. Solutions of the ideal, rotational-flow equations have been obtained, for example, by Rowe (1970) and Stuart & Hetherington (1970) and exhibit relatively strong oscillatory secondary flows of the type investigated earlier by Squire & Winter (1951) and Hawthorne (1951). The laminar flow solutions of the steady, three-dimensional, Navier–Stokes equations of Ghia & Sokhey (1977) and of Humphrey *et al.* (1977) for rectangular cross-sections and of Humphrey (1978*a*) for circular and annular cross-sections also demonstrate strong secondary flows. The latter two studies are based on elliptic forms of the transport equations and reveal, for a range of Reynolds numbers, that recirculation in the main flow direction can be present. Turbulent flow results have been obtained, for example, by Patankar *et al.* (1975) and Pratap & Spalding (1975), by solving parabolic forms of the transport equations. Thus, these authors presumed that recirculation in the planes parallel to the symmetry plane does not exist and that the flow can be represented by a two-equation turbulence model. In all cases, there is a need for experimental information to test the appropriateness of the assumptions and to help remove the present lack of understanding of the physical processes, especially in ducts of strong curvature.

In an earlier communication, Humphrey & Whitelaw (1977) presented preliminary results and brief discussion related to flows over curved surfaces and in bends. The purpose of the present contribution is to provide detailed measurements, of quantified and good precision, which will increase present understanding of the physical processes governing curved duct flows. This is partly achieved here by comparison of experimental results with elliptic calculations based on a two-equation $(k - \epsilon)$ model of turbulence. Although, as will be shown, the numerical uncertainties are significant and probably greater than those introduced by the turbulence model.

The following section describes the flow configuration and the instrumentation used to obtain the measurements. The results, including those obtained from the calculation method outlined in Appendix A and previously described, in relation to laminar-flow equations, by Humphrey *et al.* (1977), are presented in the *third* section and discussed in the *fourth*. The paper ends with brief concluding remarks.
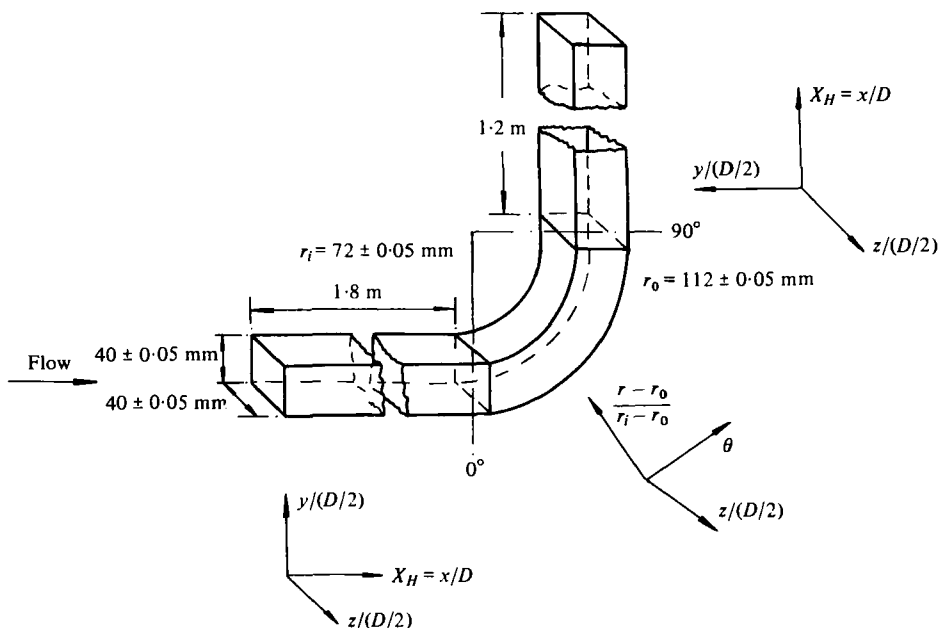
FIGURE 1. Experimental geometry of 90° bend with tangents.

2. Flow configuration, instrumentation and procedures

The flow configuration is identical to that used by Humphrey *et al.* (1977). It comprises a 90° perspex bend of mean radius $R_c = 92$ mm, see Figure 1, attached to the end of a rectangular channel previously described by Melling & Whitelaw (1976). The cross-section was $D^2 = 40 \pm 0.05 \times 40 \pm 0.05$ mm² and the bend was located in the vertical plane with a 1·2 m length of straight duct of the same cross section attached to its downstream end. The present results were obtained with a water flow of 1·42 kg/s corresponding to a Reynolds number of 4.0×10^4 and a Dean number of $De \equiv Re(\frac{1}{2}D/R_c)^{\frac{1}{2}} = 2.6 \times 10^4$.

The anemometer was similar to that described in the two previous papers. It was aligned perpendicularly to the side walls of the bend and comprised a 5 mW helium-neon laser, an optical unit of the type described by Durst & Whitelaw (1971) but modified to allow rotation of the measuring volume through 90° without the need to adjust the position of the laser, a light collection arrangement, an EMI 9558B photomultiplier and a frequency-tracking demodulator (DISA 55L20). The mean velocity, after true integration (DISA 55B30), and corresponding normal stress were obtained from a Solartron digital voltmeter and true rms meter (DISA 55D35), respectively. The control-volume dimensions were determined by the 15° angle between the transmitted light beams and the light-collection arrangement and were calculated to correspond to a length of 2·0 mm and a diameter of 0·26 mm; the discrimination level of the frequency-tracking demodulator reduced these dimensions, according to a count of fringes reproduced by scattering particles on an oscilloscope, by approximately 20 %.

Measurements of the longitudinal and radial components of mean velocity and the corresponding normal and Reynolds stresses were obtained with the single channel

| | Maximum error % | |
Variable	Systematic	Random
U_θ/U_B, U_z/U_B	0·8	1·0
U_r/U_B	1·0	2·0
$\tilde{u}_\theta/U_B$, $\tilde{u}_z/U_B$	1·0	2·0
$\tilde{u}_r/U_B$	1·7	2·8
$\overline{u_\theta u_r}/U_B^2$	2·2	5·0

<center>TABLE 1</center>

anemometer in the manner described by Humphrey (1977) and Durst, Melling & Whitelaw (1976). On average 12 traverses of 25 points each were made in planes corresponding to $-11·1$, $-6·25$ and $-2·5$ hydraulic diameters in the straight duct and at $0°$, $45°$, $71°$ and $90°$ in the bend. The cross-stream velocity and corresponding stresses were also measured in the $0°$ and $90°$ planes.

The influence of transit-time, gradient and noise broadening were examined and, as far as possible, quantified. The estimated maximum systematic and r.m.s. of the random errors are indicated in table 1. The large number of measured points allowed them to be conveniently fitted to a least-squares polynomial of the form:

$$U \text{ or } \tilde{u} = A_0 + A_1 y + A_2 z + A_3 y^2 + A_4 yz + A_5 z^2 + A_6 y^3$$
$$+ A_7 y^2 z + A_8 yz^2 + A_9 z^3 + \ldots.$$

The theory underlying this approach has been reported, for example, by Himmelblau (1970). The maximum deviations of measured points from the fits used to plot the figures of the following section, were 2 % for mean velocities and 3 % for Reynolds stresses and occurred in the flow regions close to the walls. The results on both sides of the bend symmetry plane were compared at all measurement stations and indicated random asymmetries only slightly larger than the uncertainty introduced by the fitting procedure; as a consequence, the data on the two sides were averaged and the regression applied to a symmetrical half.

3. Results and comparisons

A typical set of measurements is shown on figure 2 and represents values of the mean voltage and r.m.s. of the corresponding fluctuations in the $45°$ plane. Contours of mean velocity and Reynolds stress were obtained from a knowledge of the relationship between the measured voltage and velocity and the fitting procedure described in the previous section; they are presented in figures 3–11 for five of the seven measurement stations. Figures 3 to 7 relate to the longitudinal velocity component, figures 8 and 9 to the radial component and figures 10 and 11 to the shear stress. For comparison and discussion purposes calculated contours of mean flow properties, where appropriate, have been included in the figures.

3.1. *Mean velocities*

The measurements of longitudinal mean velocity obtained at $-11·1$, $-6·25$ and $-2·5$ hydraulic diameters from the entrance plane of the bend are within 5 % of the
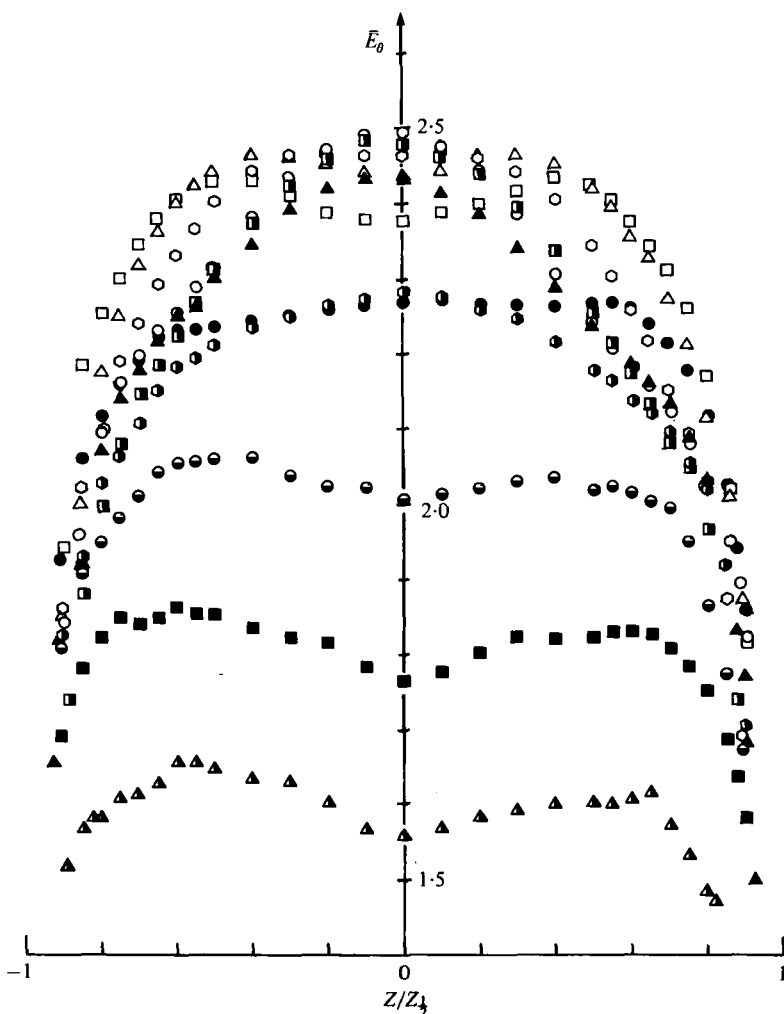
FIGURE 2 (a). For legend see page 448.

results previously reported by Melling & Whitelaw (1976) for $Re = 4.2 \times 10^4$ and at 36.8 hydraulic diameters from the inlet to the present straight duct. The measurements at $x_H = -2.5$, shown on figure 3, correspond to a location 42.5 hydraulic diameters from the duct inlet and have the general features of developed square-duct flow with no influence of the downstream bend. This is in contrast to the laminar-flow results of Humphrey *et al.* (1977) which were slightly influenced by the bend at $x_H = -2.5$. The bulging of the present contours towards the corners of the duct is caused by the normal-stress driven cross-stream flow ($< 0.02 \, U_B$) previously discussed, for example, by Gessner (1973) and Melling & Whitelaw (1976). This weak cross-stream flow is in the form of symmetric counter-rotating vortices in the duct corners and directed along the angle bisector towards the corner; it will be overcome by the much stronger pressure-driven secondary flow in the bend which takes the form of two counter-rotating longitudinal (main) vortices with a forward stagnation region at the centre-line of the outer wall.
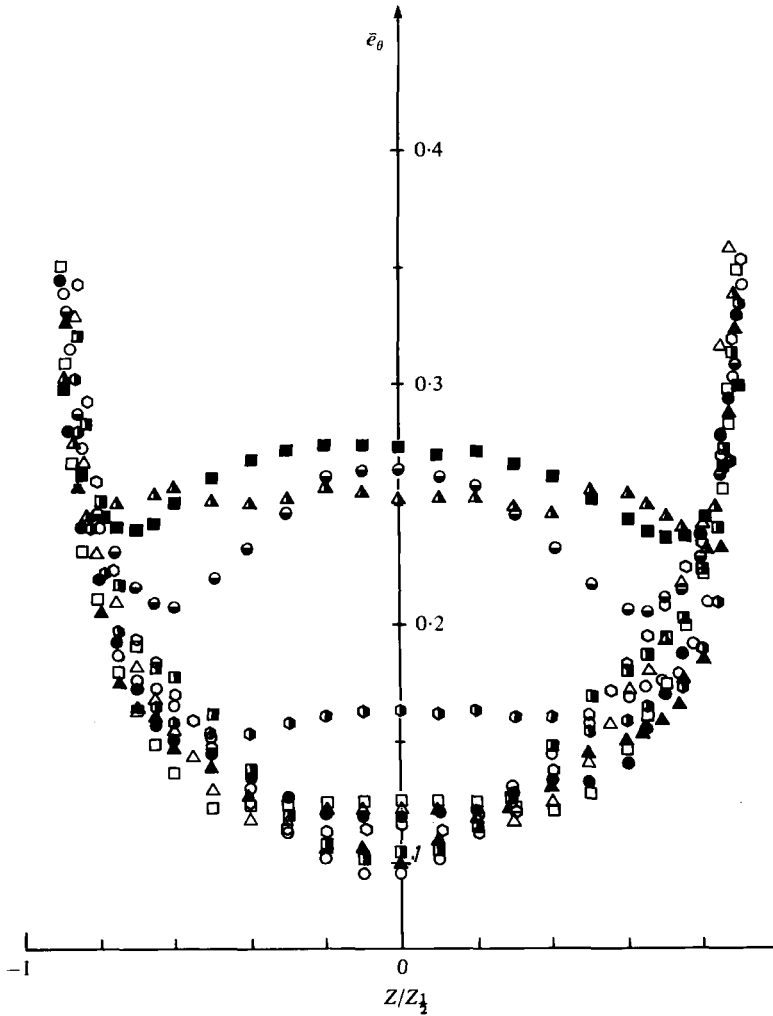
FIGURE 2. Experimental data at 45° station in turbulent bend flow. Results are typical of the degree of symmetry obtained in the flow. (a) Longitudinal velocity given in volts measured, (b) Longitudinal turbulence intensity given in volts measured. Values of $(r - r_i)/(r_0 - r_i)$: ▲, 0·92; ■, 0·84; ◓, 0·76; ◑, 0·67; ▲, 0·59; ○, 0·51; ▯, 0·43; ◯, 0·35; △, 0·26; □, 0·18; ●, 0·10.

At the inlet plane of the bend, figure 4(a), the mean longitudinal velocity contours (U_θ/U_B) display an acceleration of the fluid moving near the inner-radius wall (r_i) in accordance with the initially favourable longitudinal pressure gradient there. Simultaneously, the fluid moving near the outer-radius wall (r_0), responding to an initially unfavourable longitudinal pressure gradient, is decelerated. The longitudinal pressure gradient influencing the flow entering the bend is a consequence of the centrifugal force, radial pressure-gradient balance set up by the flow in the bend. Bulging of the U_θ contours towards the duct corners persists at the 0° plane but has been substantially reduced at the outer-radius wall, in accordance with the negative values of U_r over almost the entire cross-section as shown in figure 8(a). The effect of U_r is, therefore, to oppose normal stress-driven motion at the outer-wall corners of the bend and to favour it at the inner-wall corners.
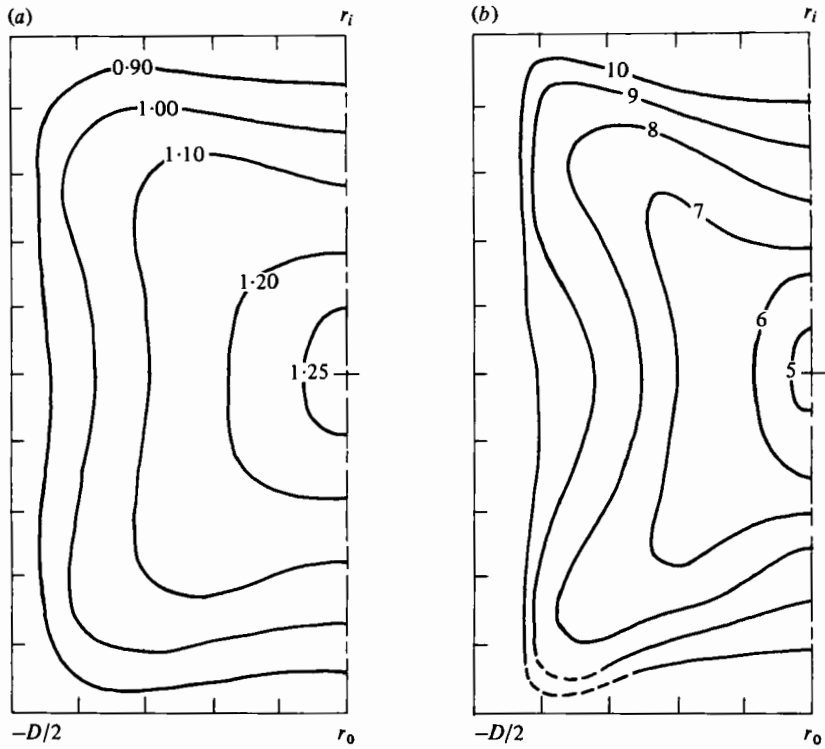
FIGURE 3. Turbulent bend flow; $x_H = -2.5$. (a) Contours of U_x/U_B. (b) Contours of $(\tilde{u}_x/U_B) \times 10^2$.
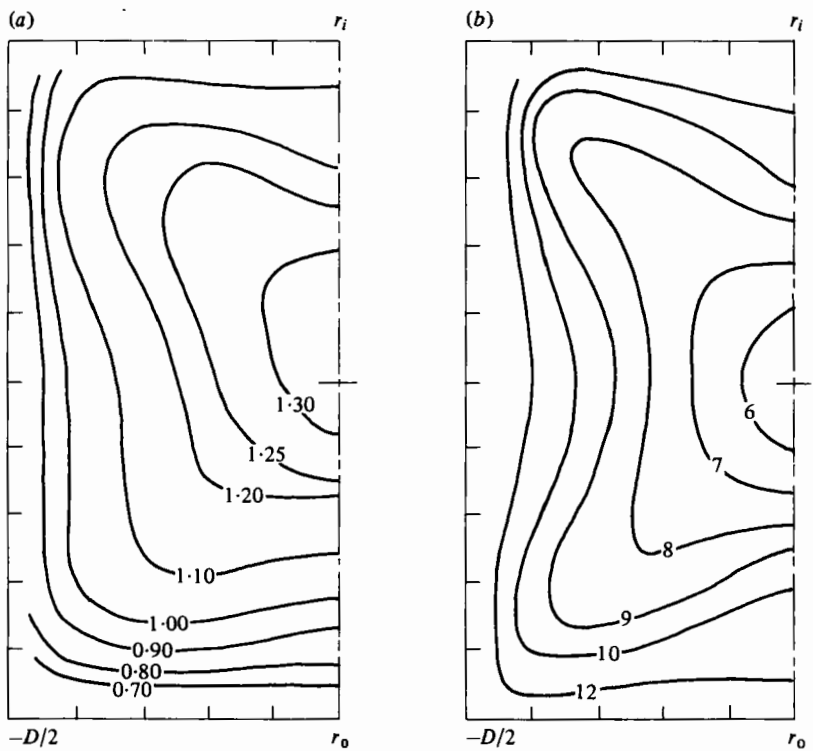

FIGURE 4. Turbulent bend flow: $\theta = 0°$, (a) Contours of U_θ/U_B. (b) Contours of $(\tilde{u}_\theta/U_B) \times 10^2$.
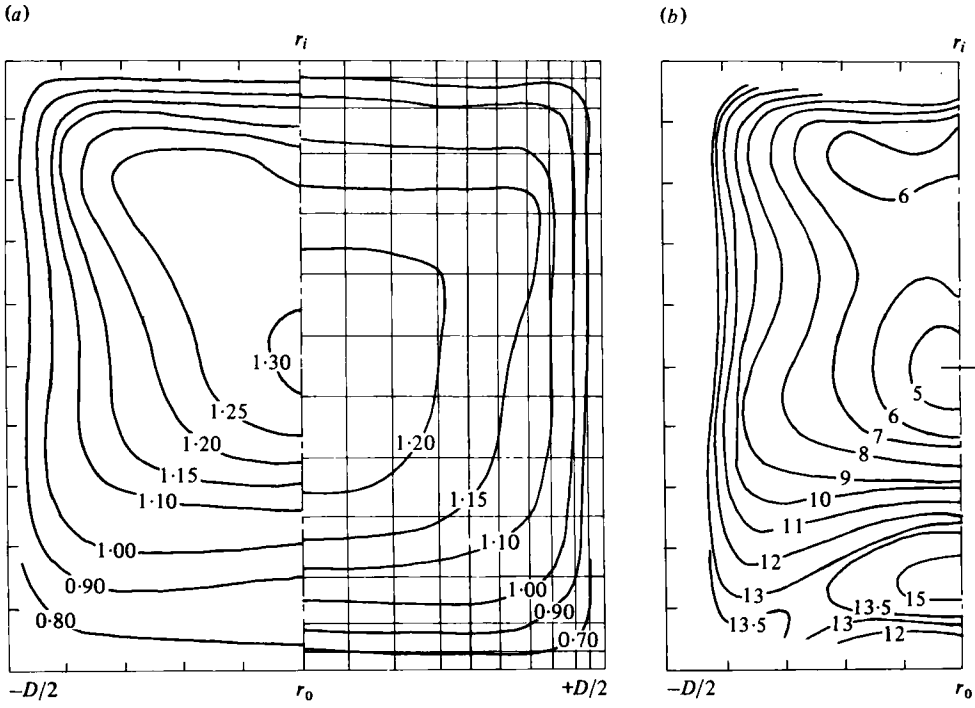
(a)

(b)

FIGURE 5. Turbulent bend flow; $\theta = 45°$. (a) Contours of U_θ/U_B with calculations on right-hand side. (b) Contours of $(\tilde{u}_\theta/U_B) \times 10^2$.

(a)

(b)

FIGURE 6. Turbulent bend flow; $\theta = 71°$. (a) Contours of U_θ/U_B with calculations on right-hand side. (b) Contours of $(\tilde{u}_\theta/U_B) \times 10^2$.
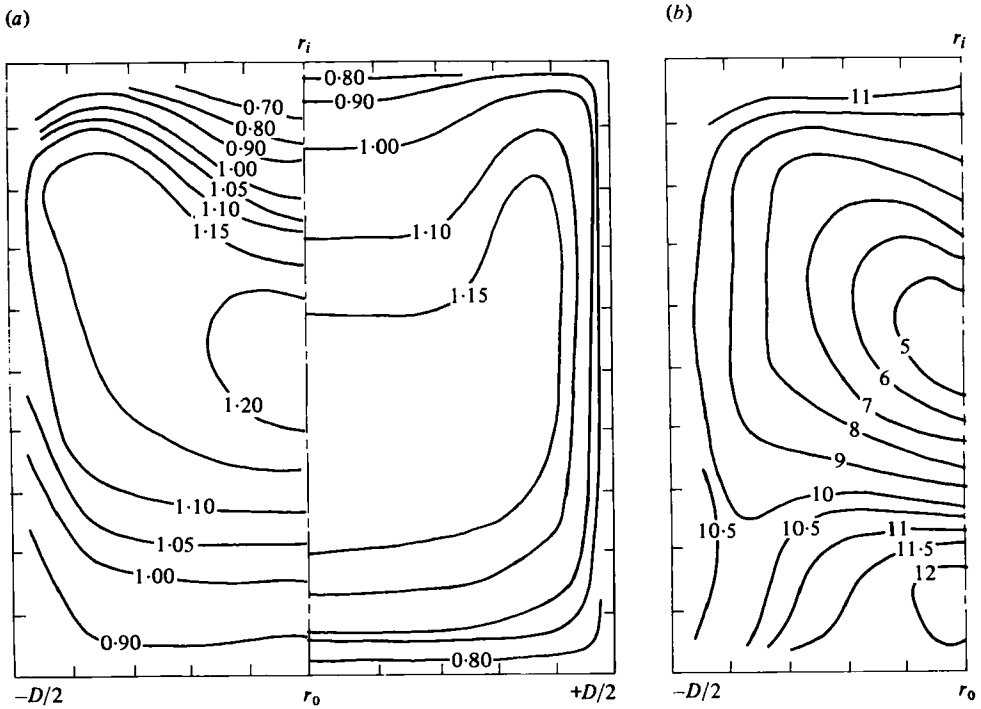
FIGURE 7. Turbulent bend flow; $\theta = 90°$. (a) Contours of U_θ / U_B with calculations on right-hand side. (b) Contours of $(\tilde{u}_\theta / U_B) \times 10^2$.

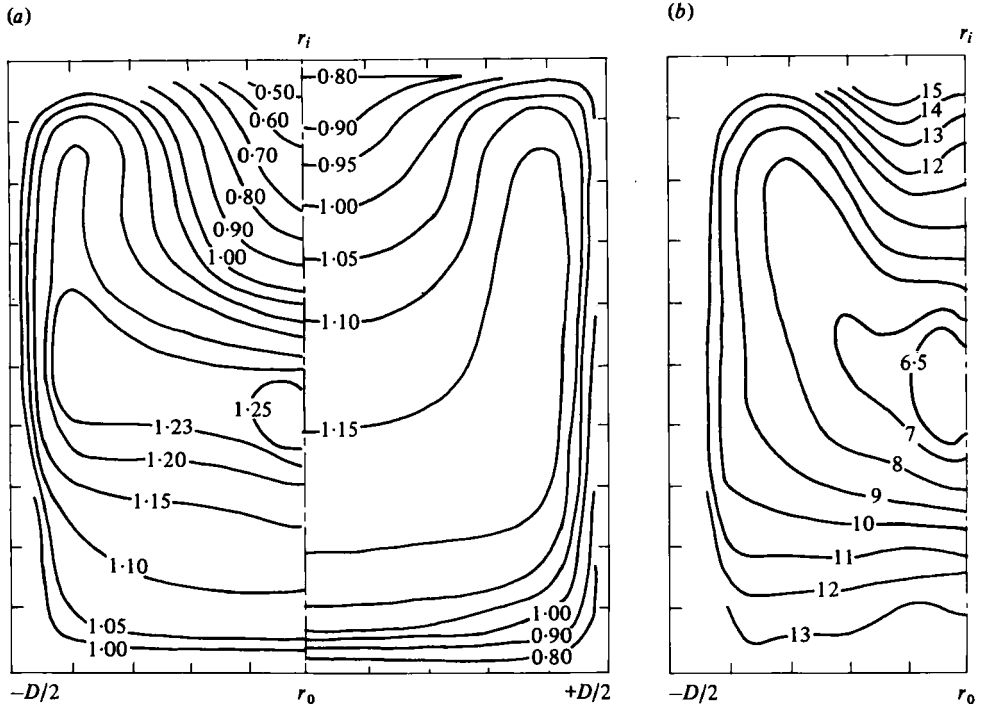FIGURE 8. Turbulent bend flow; $\theta = 0°$. (a) Contours of U_r / U_B. (b) Contours of $(\tilde{u}_r / U_B) \times 10^2$.

(a)

(b)

FIGURE 9. Turbulent bend flow; $\theta = 90°$. (a) Contours of U_r/U_B with calculations on right-hand side. (b) Contours of $(\tilde{u}_r/U_B) \times 10^2$.

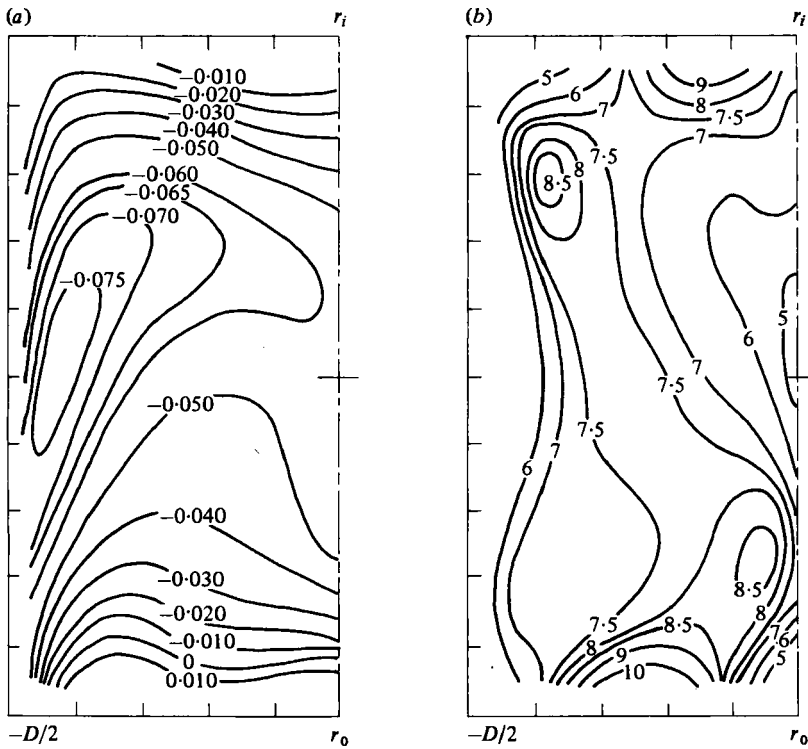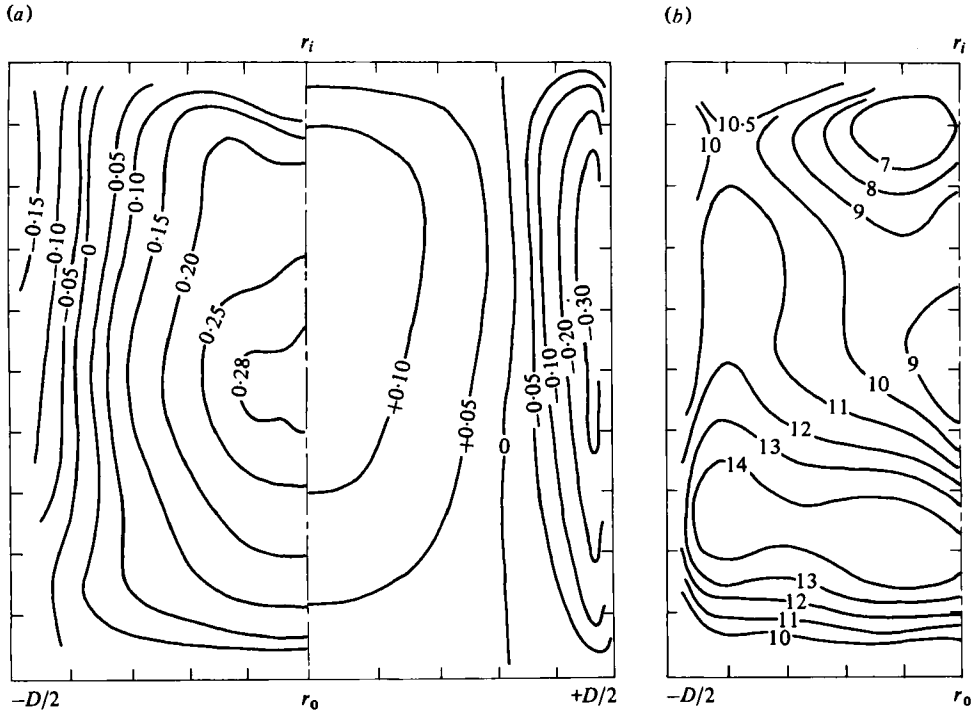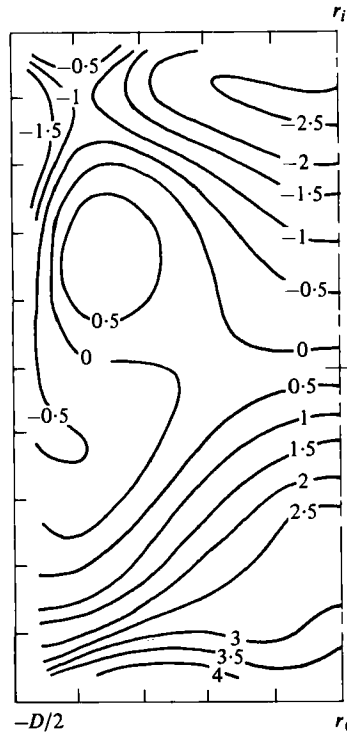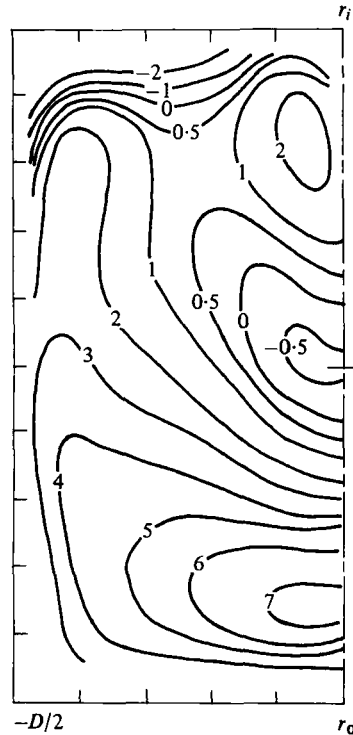FIGURE 10. Turbulent bend flows; $\theta = 0°$. Contours of $(\overline{u_\theta u_r}/U_B^2) \times 10^3$.

FIGURE 11. Turbulent bend flows for $\theta = 90°$. Contours of $(\overline{u_\theta u_r}/U_B^2) \times 10^3$.

Acceleration of the fluid near r_i displaces the maximum U_θ velocity contours towards the inner-radius wall and the effect is still noticeable at the 45° station shown in figure 5(a) with steep gradients of U_θ appearing near r_i. The distorted contours for $U_\theta/U_B = 1.20$ and 1.25, which arise in both laminar and turbulent bend flows as a result of the pressure gradient in the secondary flow plane induced by lateral curvature of the main flow, are evidence of developing pressure-driven secondary motion. At 71° and 90°, figures 6(a) and 7(a), the strong secondary motion (up to $0.28 \times U_B$ at the 90° plane) produced by the lateral curvature, causes a substantial deformation of the U_θ contours. The steep gradients in U_θ shift from r_i to r_0 with lower gradients appearing at the inner-radius wall. The results also show that high-speed flow has been increasingly displaced towards the outer-radius and side walls, whereas fluid with low velocity accumulates at the inner-radius wall of the bend.

The contours of radial velocity obtained in the inlet plane to the bend are shown on figure 8(a) and reveal secondary velocities up to $0.075 U_B$. These values are significantly larger than those associated with normal-stress-driven secondary flows and confirm the influence of the bend on the flow at the inlet. The vortex pattern, associated with normal-stress-driven secondary flows is no longer apparent although the sign changes, near to the inner and outer walls, indicate that it has not been completely overcome by the pressure forces. At 90°, figure 9(a), large secondary flows are present and the pattern conforms to a strong rotational movement in each symmetrical half of the bend with values of U_r as large as $+0.28 U_B$ along the symmetry line and $-0.15 U_B$ along the side walls.

The velocity contours, calculated at the three downstream stations display the same general characteristics as the measurements but with quantitative differences which are large. The contours of the longitudinal velocity component indicate a shift of maximum velocity which, like the measurements, is displaced slightly towards the inner wall at 45° and moves towards the outer wall for larger values of angular position. The movement is rather more rapid than the measurements and there is a general tendency for the velocity gradients to be less except in the immediate vicinity of the walls where the logarithmic wall functions control the calculations. It would appear, therefore, and consistent with the distribution of grid nodes in the cross-stream plane as shown in figure 5, that there has been some smearing in the numerical results.

It is also noticeable, at the 45° position, that the secondary flow has been slower to develop in the calculations than in the measurements. The tendency for the contours to bend into the corners, shown by the measurements, is not revealed by the calculations until the 71° station. The main features of the radial component of mean velocity, shown in figure 9, are represented by the calculation although the location of the zero-velocity line dividing the regions of positive and negative velocity is further from the side wall, the magnitude of the negative values is high and of the kinetic values too low.

3.2. *Reynolds stresses*

Turbulence intensities and shear stress measurements (normalized by U_B^2) are presented in contoured form in figures 3(b) to 9(b) and 10 and 11, respectively. As for the mean longitudinal velocity component, the pattern in the distribution of $\tilde{u}_x$ did not change significantly between $x_H = -11 \cdot 1$ and $-2 \cdot 5$ and the values for $\tilde{u}_x$ are in good agreement with the measurements of Melling & Whitelaw (1976) at their furthest downstream position.

In general, the results at the three upstream tangent stations (see figure 3b) show high values of $\tilde{u}_x$ near the duct walls, diminishing towards the core region of the flow. Distortions by the normal stress driven secondary motions are evidenced (as for U_x) by bulging of the contours towards the duct corners. At 0°, $\tilde{u}_\theta$ has been affected little by the pressure gradients affecting the longitudinal and transverse mean velocities although a slight diminution in the $\tilde{u}_\theta$ contours near r_0, relative to those at r_i, can be observed and is caused by the same mechanism which reduced bulging in the U_θ contours.

At 45°, figure 5(b) shows a dramatic alteration in the pattern for $\tilde{u}_\theta$. Relatively high levels of turbulence intensity (12% to 15%) arise near r_0 and the side walls with lower values (6% to 9%) appearing near r_i except nearer to the inner-radius wall. At 71°, the pattern is modified further with $\tilde{u}_\theta$ returning to lower values (10% to 12%) near to r_0 and the side walls but increasing (8% to 11%) near to r_i. At 90°, a complete reversal of the situation observed at 45° has emerged; values of $\tilde{u}_\theta$ are relatively large (12% to 15%) at the inner-radius wall, whereas they are lower (10% to 13%) near r_0 and the side walls. The general patterns for $\tilde{u}_\theta$ at 45°, 71° and 90° are seen to be in conformity with the sense of circulation in the secondary motion of the first kind which increases in magnitude along the bend. This appears to suggest that convection of the Reynolds stresses by the cross-stream flow becomes increasingly significant with distance through the bend.

Contour plots of $\tilde{u}_r$ at 0° and 90° are presented in figures 8(b) and 9(b) and although

the trends at 0° are in agreement with those of Melling & Whitelaw (1976) at the furthest downstream position of their square duct flow, differences can be observed. In the present case, two islands of relatively high turbulence intensity (8·5 %) have been formed at the side wall (near r_i) and near the bend symmetry plane (near r_o) respectively. These peaks are joined by a 7·5 % ridge separating two regions of lower turbulence intensity with strong gradients appearing towards the walls. At 90°, the $\tilde{u}_r$ profiles indicate a distortion which appears to stem from the strong secondary motion there.

Figures 10 and 11 present the shear stress contours $\overline{u_\theta u_r}$ at 0° and 90° respectively. At 0°, the contours in the upper half of the figure (towards r_i) present features strongly reminiscent of the developed turbulent duct flow results of Melling & Whitelaw (1976). The bottom half of the figure, however, is very different and shows a region of negative $\overline{u_\theta u_r}$, near the side wall, contained between positive values: since this region coincides with negative values of $\partial U_\theta/\partial r$, the result is a negative contribution to the generation of kinetic energy of turbulence. At 90°, the $\overline{u_\theta u_r}$ contours display distortions, caused by the secondary motion. Relatively high and positive values of $\overline{u_\theta u_r}$ are displaced towards r_0 and the side wall. Lower values of $\overline{u_\theta u_r}$, but still mainly positive, appear over a large region near r_i coinciding with positive values of $\partial U_\theta/\partial r$. As above, this represents a negative contribution to the generation of kinetic energy of turbulence and is in agreement with the stabilizing effects of the inner-radius wall on the flow.

The calculated values of turbulence energy in the exit plane are not shown for reasons of space but reflect the deficiencies of the mean-flow calculations and of the assumed turbulence model. Comparison of the calculations and the measurements of figures 7b and 9b indicates that the former are generally lower and more uniform in the central region. The calculated values of the Reynolds shear stresses are also poorly represented in detail although major features, such as the central zero contour of $\overline{u_\theta u_r}$, are reproduced.

4. Discussion

Comparisons between the present turbulent flow and the previous laminar flow of Humphrey *et al.* indicate that the normalized velocity fields are similar in magnitude although the small region of longitudinal recirculation observed in the laminar flow does not appear in the turbulent flow. A second difference relates to the locus of maximum-velocity locations which, in the turbulent flow case, are close to the centre of curvature for the first 71°. Secondary motion, arising through an imbalance between centrifugal force and radial pressure gradient at the side walls of the bend, displaces high-speed fluid towards the outer-radius wall, along the region containing the symmetry plane, and low-speed fluid towards the inner-radius wall, i.e. along the side walls: this effect is much larger in the turbulent-flow results due to the higher Dean number. The secondary motion in the turbulent case is responsible for strong cross-stream convection of Reynolds stresses and for high turbulence-energy fluid to be driven from the outer-radius wall, where turbulence is generated strongly, towards the inner-radius wall, where it can be suppressed. In turn, stabilized flow with lower level turbulence energy at the inner-radius wall is convected, by the secondary motion, along the symmetry plane into the core region of the flow and towards the outer-radius wall. Between 45° and 90°, the characteristics of the turbulent bend flow near

to the symmetry plane are similar to those observed in two-dimensional channels with curvature. The similarity diminishes, however, at larger bend angles where the secondary motion reaches values between 20 % and 30 % of the bulk average velocity. Comparison between present results and two-dimensional channel flow also shows that the former are more isotropic than the latter at the outer-radius wall. Secondary motion, driven by normal stresses and important in straight non-circular-duct flow, is negligible compared to the pressure-driven secondary flows.

Stabilizing curvature, occurring on convex walls, i.e. the inner-radius wall of the bend, has the effect of lowering Reynolds shear stresses and turbulence energy levels in comparison to otherwise equivalent straight shear-layer flows. The results for $\tilde{u}_\theta$ at 45° and $\tilde{u}_r$ and $\overline{u_\theta u_r}$ at 90° show this effect clearly as do previous results for two-dimensional curved flows. The decrease in turbulence is associated with a corresponding decrease in static pressure in the flow direction and hence acceleration of the flow. This is in agreement with the larger levels for U_θ measured near the inner-radius wall at 0° and 45°. Destabilizing curvature appears at concave walls, i.e. the outer-radius wall of the bend, and results in unusually high levels of Reynolds shear stresses and turbulence kinetic energy. This accounts for the relatively large values of the stresses at the outer-radius wall of the bend.

The comparison between the better known behaviour of curved two-dimensional channel flow and present experimental results helps to explain some of the characteristics of bend flow. In the three-dimensional flow, however, the cross-stream vortical motion is responsible for the transport of energy containing eddies along the side walls of the bend from the concave (destabilizing) to the convex (stabilizing) surface, and is partly the cause of the high levels of Reynolds stresses which appear at the side walls. In turn, fluid elements in which the turbulence has been suppressed are displaced along the bend symmetry plane from the inner-radius wall into the core region of the flow by the secondary motion. At the same time, pressure strain redistribution between normal stress components, turbulent diffusion and dissipation, all affect the distribution of the stresses throughout the flow. A result is for regions of relatively strong anisotropy to occur in the bend. For example, at 0° and near the side walls, $1 < \overline{u_\theta^2}/\overline{u_r^2} < 4$ and $-0.2 < \overline{u_\theta u_r}/\overline{u_r^2} < 0.4$. At 90° and near the inner-radius wall, $1.6 < \overline{u_\theta^2}/\overline{u_r^2} < 4.6$ and $0.1 < \overline{u_\theta u_r}/\overline{u_r^2} < 0.5$, whereas at the outer-radius wall, $0.5 < \overline{u_\theta^2}/\overline{u_r^2} < 1.4$ and $0.3 < \overline{u_\theta u_r}/\overline{u_\theta^2} < 0.4$: these results at 90° indicate that the flow at the outer-radius wall is more isotropic than that at the inner-radius wall. This observation is in agreement with the results of Eskinazi & Yeh (1956) who found $4 < \overline{u_\theta^2}/\overline{u_r^2} < 5.8$ at the inner-radius wall and $3 < \overline{u_\theta^2}/\overline{u_r^2} < 4.4$ at the outer-radius wall for fully-developed curved two-dimensional channel flow. The comparison also shows that a higher degree of isotropy is attained at the outer-radius wall of a fully three-dimensional bend flow than at the corresponding wall of a two-dimensional curved channel flow.

Analysis of the Reynolds-stress equations, which include effects due to convection, pressure strain, turbulent diffusion and dissipation, would benefit understanding of the present anisotropic flow but is hampered by the incompleteness of the measurements and their precision. A simplified analysis of the generation terms in the normal stress equations based on the assumption of local equilibrium conditions near walls and provided in detailed form by Humphrey (1977) is in close accord with the measured distribution of $\tilde{u}_r$ at 0° and 90°, but not with that of $\tilde{u}_\theta$ at 90° due, in part, to

the neglect of $\partial U_\theta/\partial\theta$ in the analysis. The experimental results indicate that convective transport of $\overline{u_\theta^2}$ into the inner-wall region of the bend flow (from the outer and side wall locations) increases the level of $\overline{u_\theta^2}$ (at the inner wall region) at a faster rate than it is suppressed or dissipated. In regions where $\overline{u_r^2}$ and $\overline{u_\theta^2}$ are suppressed, the Reynolds stresses act on the mean momentum gradients to return energy to the mean flow and accounts for the displacement between positions of maximum velocity and zero shear stress.

The complexity of the turbulence characteristics of the flow implies that the eddy-viscosity hypothesis will give rise to errors. Detailed features, such as negative production and the influence of the individual normal stresses are clearly not represented although, for example, the calculated gradual displacement of the peak value of $\tilde{u}_\theta$ from the outer to inner wall is in accord with measurement. The mean flow is however very strongly influenced by the pressure forces and is unlikely to be strongly influenced by the turbulence model. In addition, the representation of the flow by less than 3200 discrete nodes is bound to give rise to numerical errors which may be large, in comparison with those caused by the turbulence model. The storage requirement of the computer limited the number of nodes which could be used with the present program and precluded calculations with a more refined grid. Similarly, the extensive run times and related costs allowed only a small number of tests with different distributions of nodes.

The calculations for U_θ along the bend symmetry plane (especially near the inner-radius wall) do not show the strong influence that secondary motion has on the corresponding experimental variables. This discrepancy is certainly related to the finite numbers of nodes which result in numerical diffusion in the calculations. An estimate of the magnitude of the numerical diffusion, relative to turbulent diffusion, may be obtained from the expression

$$\mu_{\text{num}}/\mu_{\text{eff}} \simeq 0.36\, R_c \left(\frac{\mu}{\mu_{\text{eff}}}\right) \sin 2\alpha,$$

where $R_c = V\rho h/\mu$ is the cell Reynolds number based upon the distance between nodes, h, and α is the angle that the velocity vector makes with the co-ordinate system. Calculated values for $\mu_{\text{num}}/\mu_{\text{eff}}$ show that, contrary to the case for the cross-stream flow, longitudinal numerical diffusion was probably significant in the bend. Thus, in the main flow direction, values $\mu_{\text{num}}/\mu_{\text{eff}}$ of up to 6 were obtained near the side and inner-radius walls and along the symmetry plane in the bend. These are precisely the locations where U_θ and U_r disagree most with the measurements. Adjustment of the grid nodes to lower the value of cell Reynolds number in this region inevitably increased it elsewhere and significant improvements could not be obtained with the total number of nodes available. Calculations, with the same initial conditions and a turbulent viscosity of zero, gave rise to a similar pattern of results near the inner radius; this suggests that, in this region, the numerical diffusion strongly affects the present flow.

It is also possible that the assumed initial conditions may have contributed to the discrepancies between measurements and calculations. For this reason,† the calculations were repeated with initial conditions assigned at $X_H = -3.75$ and with dependent variables corresponding to the fully-developed flow of Melling. The number of

† As well as at the suggestion of a referee.

nodes in the bend flow was as before and the calculations in the upstream tangent were prepared in the same manner as previously reported by Humphrey *et al.* The resulting calculated values of mean velocity were similar, in their general characteristics, to those obtained with the initial conditions described in the appendix and assigned in the plane of the bend entrance. The discrepancies between the measurements and calculations were of the same magnitude as those indicated by figures 4(a), 5(a), 6(a) and 7(a) and there was a tendency for the central region of uniform velocity to increase slightly towards the inner wall.

The numerical deficiencies associated with regions ot the present flow, the limited availability of grid nodes and the elliptic differential equations, raise the question of the relative advantages of parabolic equations or partially elliptic equations $[P = P(\theta, r, z)$ but $\partial^2/\partial\theta^2 = 0]$. The reduced equation forms have reduced storage requirements and the number of nodes can be increased significantly with consequent decrease in numerical error. Their use implies, however, that longitudinal diffusion is unimportant and this cannot always be known *a priori*. In the laminar-flow results of Humphrey *et al.* (1977), for example, they would have ruled out the possibility of the recirculation region observed experimentally. In the present case, the magnitude of longitudinal diffusion could not be adequately assessed from the experimental results at the 45°, 71° and 90° locations in the bend although low values of U_θ near the inner-radius wall suggested that it could be significant. Subsequently, the turbulent flow calculations indicated that, even though $\partial P/\partial\theta$ is large, longitudinal diffusion is not larger than 2 % of longitudinal convection in the present geometry. It would appear, therefore, that a semi-elliptic procedure accounting for strong pressure variations could provide more precise results through increased grid refinement. However, this probability will certainly decrease with increasing Dean numbers.

6. Concluding remarks

The main effect of the bend on the flow passing through it is to induce strong cross-stream motions which develop into a pair of counter-rotating vortices in the longitudinal direction. The driving force for this secondary motion is the centrifugal force-radial pressure gradient imbalance which acts upon the slowly moving fluid along the side walls of the bend, and displaces it along the side walls from the outer to inner curvature wall. Continuity requires that a corresponding motion displace fluid along the bend symmetry plane from the inner to the outer curvature wall. The cross-stream flow is weak at first ($\simeq 0.07\ U_B$) but progressively gains momentum until it attains values $\lesssim 0.28\ U_B$ at the 90° plane. As a result of the strong cross-stream motion, high speed flow accumulates at the outer wall of the bend and low speed flow at the inner wall. Likewise, the secondary motion is responsible for *cross-stream convection of the stresses*. This pressure driven cross-stream flow is more than an order of magnitude larger than the cross-stream flow which arises due to the normal stress imbalances.

Secondary motion driven by the normal stresses does exist and is responsible for bulging of the velocity contours towards the duct corners in the upstream section connected to the bend. Its effects are, however, overwhelmed by the pressure-driven secondary flow before the 45° station has been reached.

The results may be compared with the previous laminar-flow data obtained in the

same bend at a lower Dean number. In the present case, there is no region of longitudinal flow recirculation although the velocity gradients do indicate a region of low wall-shear stress at the inner-radius wall and in the latter part of the bend. This is consistent with the locus of maximum velocity positions which corresponds to the mean radius until the 71° station where it begins to move towards the outer wall. In the laminar-flow case, the locus of maximum velocity positions moves rapidly toward the outer wall from the beginning of the bend and tends to stay there. It may be expected that large differences may exist in the geometric configuration for other changes in the initial conditions. For example, the use of a shorter region of the straight inlet duct, with corresponding thin boundary layers and a core region of potential flow, can be expected to behave in a manner consistent with potential flow solutions for a significant region of the bend. Thus, in such a case, the locus of maximum-velocity-positions will move rapidly to the inner wall and will move out again at a downstream location where the boundary layers have thickened and provided slower moving fluid which can be more rapidly driven into a secondary flow pattern.

In general, the stress measurements show high values near the walls, where shearing is greatest, diminishing towards the core of the flow. Stabilizing effects due to convex curvature at the inner wall of the bend are responsible for lowering the turbulence intensity there whereas destabilizing concave curvature effects at the outer wall raises it. A consequence of the secondary motion is an interchange of turbulence energy between the inner and outer wall; this serves to counteract the stabilizing and destabilizing effects of these walls, respectively. The result is a highly anisotropic complex pattern of stresses. In agreement with two-dimensional channel flows, the measurements indicate a higher level of anisotropy at the destabilizing outer wall than at the stabilizing inner wall. However, the present bend flow is more isotropic at the outer-radius wall than the channel flow. Regions of negative contribution to the kinetic energy of turbulence arise at both the 0° and 90° planes and are responsible for returning energy from the turbulent motion to the mean flow. As a consequence, displacements between positions of maximum velocity and zero shear stress can arise.

Eddy viscosity models of turbulence are unable to represent negative contributions to the generation of kinetic energy of turbulence. However, because changes in the bend flow are governed primarily by pressure gradient effects, an eddy viscosity formulation, preferably which allows for transport of turbulence properties, may adequately allow the description of the bulk features of this flow. Accurate representation of the stress distributions will require modelling based on solutions of the Reynolds stress equations and the present data will assist evaluation of this approach.

It should be emphasized that the choice of equation form is important in flows of the present type. Although longitudinal diffusion is probably small enough to be neglected in the present geometry and, hence, allow the use of semi-elliptic calculation schemes, its effects will become increasingly important as the mean radius of curvature is decreased or the Dean number increases. The three-dimensional Navier–Stokes equations are appropriate to the present flow but, as shown here, their solution is subject to numerical inaccuracy which limits the complexity of turbulence model which can be justified. A discussion of the relative merits of possible turbulence models is probably academic in view of the degree of pressure gradient control and numerical uncertainty associated with the finite number of discrete nodes.

Appendix A

Equations, boundary conditions and calculation method

Numerical calculations of the curved duct flow are based on the elliptic form of the time averaged Navier–Stokes equations in cylindrical co-ordinates. Thus, for steady, incompressible, isothermal flow, the differential equations for continuity and momentum, with an eddy-viscosity assumption, are given by:

Continuity

$$\frac{\partial U_r}{\partial r} + \frac{1}{r}\frac{\partial U_\theta}{\partial \theta} + \frac{\partial U_z}{\partial z} + \frac{U_r}{r} = 0. \tag{1}$$

Momentum

$$\rho\left[U_r\frac{\partial U_r}{\partial r} + \frac{U_\theta}{r}\frac{\partial U_r}{\partial \theta} + U_z\frac{\partial U_r}{\partial z} - \frac{U_\theta^2}{r}\right] = -\frac{\partial P}{\partial r} = \frac{1}{r}\frac{\partial}{\partial r}\left(\mu_{\text{eff}}\, r\,\frac{\partial U_r}{\partial r}\right)$$

$$+\frac{1}{r}\frac{\partial}{\partial \theta}\left(\mu_{\text{eff}}\frac{1}{r}\frac{\partial U_r}{\partial \theta}\right) + \frac{\partial}{\partial z}\left(\mu_{\text{eff}}\frac{\partial U_r}{\partial z}\right) - \mu_{\text{eff}}\frac{U_r}{r^2} - \frac{2}{r^2}\mu_{\text{eff}}\frac{\partial U_\theta}{\partial \theta} + S_r; \tag{2}$$

$$\rho\left[U_r\frac{\partial U_\theta}{\partial r} + \frac{U_\theta}{r}\frac{\partial U_\theta}{\partial \theta} + U_z\frac{\partial U_\theta}{\partial z} + \frac{U_r U_\theta}{r}\right] = -\frac{1}{r}\frac{\partial P}{\partial \theta} + \frac{1}{r}\frac{\partial}{\partial r}\left(\mu_{\text{eff}}\, r\,\frac{\partial U_\theta}{\partial r}\right)$$

$$+\frac{1}{r}\frac{\partial}{\partial \theta}\left(\frac{\mu_{\text{eff}}}{r}\frac{\partial U_\theta}{\partial \theta}\right) + \frac{\partial}{\partial z}\left(\mu_{\text{eff}}\frac{\partial U_\theta}{\partial z}\right) - \mu_{\text{eff}}\frac{U_\theta}{r^2} + \frac{2}{r^2}\mu_{\text{eff}}\frac{\partial U_r}{\partial \theta} + S_\theta; \tag{3}$$

$$\rho\left[U_r\frac{\partial U_z}{\partial r} + \frac{U_\theta}{r}\frac{\partial U_z}{\partial \theta} + U_z\frac{\partial U_z}{\partial z}\right] = -\frac{\partial P}{\partial z} + \frac{1}{r}\frac{\partial}{\partial r}\left(\mu_{\text{eff}}\, r\,\frac{\partial U_z}{\partial r}\right)$$

$$+\frac{1}{r}\frac{\partial}{\partial \theta}\left(\mu_{\text{eff}}\frac{1}{r}\frac{\partial U_z}{\partial \theta}\right) + \frac{\partial}{\partial z}\left(\mu_{\text{eff}}\frac{\partial U_z}{\partial z}\right) + S_z; \tag{4}$$

where

$$S_r = \frac{1}{r}\frac{\partial}{\partial \theta}\left(\mu_t\, r\,\frac{\partial}{\partial r}\left(\frac{U_\theta}{r}\right)\right) + \frac{1}{r}\frac{\partial}{\partial r}\left(\mu_t\, r\,\frac{\partial U_r}{\partial r}\right) + \frac{\partial}{\partial z}\left(\mu_t\frac{\partial U_z}{\partial r}\right) - \mu_t\frac{U_r}{r^2};$$

$$S_\theta = \frac{1}{r}\frac{\partial}{\partial \theta}\left(\mu_t\left(2\frac{U_r}{r} + \frac{1}{r}\frac{\partial U_\theta}{\partial \theta}\right)\right) + \frac{\partial}{\partial r}\left(\frac{\mu_t}{r}\left(\frac{\partial U_r}{\partial \theta} - U_\theta\right)\right) + \frac{\partial}{\partial z}\left(\frac{\mu_t}{r}\frac{\partial U_z}{\partial \theta}\right) + \frac{\mu_t}{r}\left(\frac{\partial U_\theta}{\partial r} - \frac{U_\theta}{r}\right);$$

$$S_z = \frac{1}{r}\frac{\partial}{\partial \theta}\left(\mu_t\frac{\partial U_\theta}{\partial z}\right) + \frac{1}{r}\frac{\partial}{\partial r}\left(\mu_t\, r\,\frac{\partial U_r}{\partial z}\right) + \frac{\partial}{\partial z}\left(\mu_t\frac{\partial U_z}{\partial z}\right)$$

and

$$\mu_{\text{eff}} = \mu + \mu_t \simeq \mu.$$

The turbulent viscosity, μ_t, is assumed to be determined uniquely by the local values of density ρ, turbulent kinetic energy k, and a turbulent length scale l. At high

Reynolds numbers l is proportional to $k^{\frac{3}{2}}/\epsilon$, where ϵ is the rate of dissipation of turbulent kinetic energy and thus

$$\mu_t = C_\mu \rho k^2/\epsilon, \tag{5}$$

where C_μ has the constant value given below. The spatial variation of μ_t is determined by solving transport equations for k and ϵ in cylindrical co-ordinates, readily derived from the general tensor equations given by Bryant & Humphrey (1976), i.e.:

$$\rho \left[U_r \frac{\partial k}{\partial r} + \frac{U_\theta}{r} \frac{\partial k}{\partial \theta} + U_z \frac{\partial k}{\partial z} \right] = \frac{1}{r} \frac{\partial}{\partial r} \left(\frac{\mu_{\text{eff}}}{\sigma_k} r \frac{\partial k}{\partial r} \right) + \frac{1}{r^2} \frac{\partial}{\partial \theta} \left(\frac{\mu_{\text{eff}}}{\sigma_k} \frac{\partial k}{\partial \theta} \right) + \frac{\partial}{\partial z} \left(\frac{\mu_{\text{eff}}}{\sigma_k} \frac{\partial k}{\partial z} \right) + G - \rho\epsilon, \tag{6}$$

and

$$\rho \left[U_r \frac{\partial \epsilon}{\partial r} + \frac{U_\theta}{r} \frac{\partial \epsilon}{\partial \theta} + U_z \frac{\partial \epsilon}{\partial z} \right] = \frac{1}{r} \frac{\partial}{\partial r} \left(\frac{\mu_{\text{eff}}}{\sigma_\epsilon} r \frac{\partial \epsilon}{\partial r} \right) + \frac{1}{r^2} \frac{\partial}{\partial \theta} \left(\frac{\mu_{\text{eff}}}{\sigma_\epsilon} \frac{\partial \epsilon}{\partial \theta} \right)$$

$$+ \frac{\partial}{\partial z} \left(\frac{\mu_{\text{eff}}}{\sigma_\epsilon} \frac{\partial \epsilon}{\partial z} \right) + C_{\epsilon 1} \frac{\epsilon}{k} G - C_{\epsilon 2} \rho \frac{\epsilon^2}{k}, \tag{7}$$

with

$$G = \mu_t \left\{ 2 \left[\left(\frac{\partial U_r}{\partial r} \right)^2 + \left(\frac{1}{r} \frac{\partial U_\theta}{\partial \theta} \right)^2 + \left(\frac{\partial U_z}{\partial z} \right)^2 - \frac{U_\theta}{r} \left(\frac{1}{r} \frac{\partial U_r}{\partial \theta} + \frac{\partial U_\theta}{\partial r} \right) \right. \right.$$

$$+ \frac{U_r}{r} \left(\frac{U_r}{r} + \frac{2}{r} \frac{\partial U_\theta}{\partial \theta} \right) + \frac{1}{r} \left(\frac{\partial U_r}{\partial \theta} \frac{\partial U_\theta}{\partial r} + \frac{\partial U_z}{\partial \theta} \frac{\partial U_\theta}{\partial z} \right) + \frac{\partial U_r}{\partial z} \frac{\partial U_z}{\partial r} \right]$$

$$\left. + \left(\frac{U_\theta}{r} \right)^2 + \left(\frac{\partial U_\theta}{\partial r} \right)^2 + \left(\frac{\partial U_\theta}{\partial z} \right)^2 + \left(\frac{1}{r} \frac{\partial U_r}{\partial \theta} \right)^2 + \left(\frac{\partial U_r}{\partial z} \right)^2 + \left(\frac{\partial U_z}{\partial r} \right)^2 + \left(\frac{1}{r} \frac{\partial U_z}{\partial \theta} \right)^2 \right\}. \tag{8}$$

The constants in these equations were taken as $C_\mu = 0.09$, $C_{\epsilon 1} = 1.47$, $C_{\epsilon 2} = 1.92$, $\sigma_k = 1.0$ and $\sigma_\epsilon = 1.3$, in accordance with the recommendations of Patankar *et al.* (1975).

It is required to solve equations 1–7 together with appropriate boundary conditions. At the inlet plane ($\theta = 0°$), U_θ and U_r velocity components were specified from measurements of this work. In the absence of experimental information, U_z was set to zero and is a good approximation since the cross-stream flow in the bend is initially weak. The entrance distribution of k was also estimated from the measurements of $\overline{u_\theta^2}$ and $\overline{u_r^2}$ and ϵ was taken proportional to $k^{\frac{3}{2}}/l$, with l a fraction of the duct hydraulic diameter. At the exit plane ($\theta = 90°$), fully developed flow conditions were imposed by setting $\partial/\partial\theta = 0$ for all variables; this approximation has been discussed by Humphrey (1978a) in relation to laminar flow and, for the flow of interest here, is adequate since calculations with this condition applied at $\theta = 90°$ and $110°$ showed negligible differences in the mean velocity results at $\theta = 90°$. Along the bend symmetry plane, the condition $\partial/\partial z = 0$ was imposed for all variables except U_z which was set equal to zero.

Zero velocity was assumed on all solid surfaces and the region between the numerical node P, closest to the wall, and the wall was bridged by the logarithmic velocity profile:

$$U_p/(\tau_w/\rho)^{\frac{1}{2}} = A \ln \left(y_p (\tau_w/\rho)^{\frac{1}{2}}/\nu \right) + B, \tag{9}$$

τ_w is the shear stress at the wall, and y_p is the distance between the first grid node and the wall. The log-law constants were taken as $A = 2.39$ and $B = 5.45$ and U_p as the

resultant velocity at P, assumed parallel to the wall shear stress. Assuming that generation and dissipation of turbulence kinetic energy are in balance in the fluid layer between node P and the wall and using the log-law relation yields:

$$\tau_w \simeq \tau_p = \frac{\rho C_\mu^{\frac{1}{4}} k_p^{\frac{1}{2}} U_p}{A \ln \{y_p C_\mu^{\frac{1}{4}} k_p^{\frac{1}{2}} / \nu\} + B}. \tag{10}$$

The near-wall kinetic energy of turbulence, k_p, was found from its normal transport equation with diffusion set equal to zero and generation term in accord with the wall shear stress (10). The value of the dissipation of kinetic energy near the wall was determined by requiring that the turbulence length scale vary linearly with distance from the wall. Thus, substitution of $(\partial U / \partial y)_p$, obtained from (9), into a simplified kinetic energy of turbulence equation for the near-wall regions (assuming generation equals dissipation) yields the expression:

$$\epsilon_p = A \frac{C_\mu^{\frac{3}{4}} k_p^{\frac{3}{2}}}{y_p}. \tag{11}$$

The calculation algorithm used to solve the preceding equations is an extension of the numerical procedure developed and applied by Humphrey *et al.* (1977) for the prediction of laminar flow in curved ducts of rectangular cross-section. Generalization of the procedure to arbitrary orthogonal co-ordinates and its application to developing curved pipe flows of strong curvature have been documented by Humphrey (1978a). Information of the transport equations in finite difference form, their numerical solution and results for various test cases can be found in the above two references and (in more detail) in Humphrey (1977). A summary of the essential features characterizing the turbulent flow calculation method is given below.

The finite difference equations were obtained by integrating the conservation equations over volume elements or 'cells' discretizing the flow domain. The velocity components, pressure, kinetic energy of turbulence and its rate of dissipation are the dependent variables computed on a number of staggered, interconnected grids, each of which is associated with a specific variable. The general form of the finite difference expressions is given by:

$$\phi_p = \left(\sum_{i=1}^{6} A_i \phi_i + S_o \right) \bigg/ \sum_{i=1}^{6} A_i \tag{12}$$

where ϕ_p (any one of the dependent variables) is solved at a position P in the discretized flow domain. The A_i coefficients are determined at the cell surfaces and represent the combined contributions of convection and diffusion to the balance of ϕ. Other contributions arising from pressure, body forces, etc. (sources or sinks) are contained in S_o. Detailed forms for S_o in variable property flows are given by Humphrey (1978b). Solution of the system of finite difference transport equations with appropriately differenced boundary conditions is achieved by means of a cyclic series of predictor-corrector operations. The method involves using an initial or intermediate value of the pressure field to solve for an intermediate velocity field. A pressure correction to the pressure field is determined by bringing intermediate velocities into conformity with continuity. After corrections to the pressure and velocity fields are applied, the transport equations for kinetic energy of turbulence and its rate of dissipation are solved. Within each iteration, various sweeps of the entire flow domain are performed in alternate directions perpendicular to the main flow direction. The

above steps are repeated until a pre-established convergence criterion is satisfied; for example, that the largest of any of the normalized residuals be less than 10^{-3}.

Numerical computations were performed mainly with an unequally spaced grid of $14 \times 11 \times 19$ nodes $(r \times z \times \theta)$ requiring $164\,k_8$ words of CDC 7600 computer storage. The calculation time per node per dependent variable per iteration was 8×10^{-5} seconds and a run with the above node distribution and convergence criteria required 400 iterations and, as a result, 380 s.

REFERENCES

BRADSHAW, P. 1973 Effects of streamline curvature on turbulent flow. *AGARDograph* 169.

BRYANT, D. & HUMPHREY, J. A. C. 1976 Conservation equations for laminar and turbulent flows in general three-dimensional curvilinear co-ordinates. *Imperial College, Mech. Engng Rep.* no. CHT/76/6.

DURST, F. & WHITELAW, J. H. 1971 Integrated optical units for laser anemometry. *J. Phys.* E **4**, 804.

DURST, F., MELLING, A. & WHITELAW, J. H. 1976 *Principles and Practice of Laser-Doppler Anemometry.* Academic.

ESKINAZI, S. & YEH, H. 1956 An investigation on fully-developed turbulent flows in a curved channel. *J. Aero. Sci.* **23**, 23.

GESSNER, F. B. 1973 The origin of secondary flow in turbulent flow along a corner. *J. Fluid Mech.* **58**, 1.

GHIA, K. N. & SOKHEY, J. S. 1977 Laminar incompressible viscous flow in curved ducts of regular cross sections, *Trans. A.S.M.E.* I, *J. Fluids Engng* **99**, 640.

HAWTHORNE, W. R. 1951 Secondary circulation in fluid flow. *Proc. Roy. Soc.* A **206**, **374**.

HIMMELBLAU, D. M. 1970 *Process Analysis by Statistical Methods.* Wiley.

HUMPHREY, J. A. C. 1977 Flow in ducts with curvature and roughness. Ph.D. thesis, University of London.

HUMPHREY, J. A. C. 1978*a* Numerical calculation of developing laminar flow in pipes of arbitrary curvature radius. *Can. J. Chem. Eng.* **56**, 151.

HUMPHREY, J. A. C. 1978*b* Numerical calculation of variable property flows in curvilinear orthogonal coordinates, *Can. J. Chem. Eng.* **56**, 624.

HUMPHREY, J. A. C., TAYLOR, A. M. K., & WHITELAW, J. H. 1977 Laminar flow in a square duct of strong curvature. *J. Fluid Mech.* **83**, 509.

HUMPHREY, J. A. C. & WHITELAW, J. H. 1977 Measurements in curved flows. *Turbulence in Internal Flows* (edited by S. N. B. Murthy). Hemisphere.

JOHNSTON, J. P. 1976 Internal flows. In *Turbulence* (ed. P. Bradshaw), Topics in Applied Physics, vol. 19. Springer.

MELLING, A. & WHITELAW, J. H. 1976 Turbulent flow in a rectangular duct. *J. Fluid Mech.* **78**, 289.

MORI, Y., UCHIDA, Y. & UKON, J. 1971 Forced convective heat transfer in a curved channel with a square cross-section. *Int. J. Heat Mass Transfer* **14**, 1787.

PATANKAR, S. V., PRATAP, V. S. & SPALDING, D. B. 1975 Prediction of turbulent flow in curved pipes. *J. Fluid Mech.* **67**, 583.

PIERCE, F. J. & DUERSON, S. H. 1975 Reynolds stress tensors in an end wall three-dimensional channel boundary layer. *Trans. A.S.M.E.* I, *J. Fluids Engng* **97**, 618.

PRATAP, V. S. & SPALDING, D. B. 1975 Numerical computations of the flow in curved ducts. *Aero. Quarterly* **26**, 219.

ROWE, M. 1970 Measurements and computations of flow in pipe bends. *J. Fluid Mech.* **43**, 771.

SQUIRE, H. B. & WINTER, K. G. 1951 The secondary flow in a cascade of airfoils in a non-uniform stream. *J. Aero. Sci.* **18**, 271.

STUART, A. R. & HETHERINGTON, R. 1970 The solution of three-variable duct flow equations. *Proc. Int. Symp. on Fluid Mech. for the Design of Turbomachinery, Penn. State University.*

WARD-SMITH, A. J. 1971 *Pressure Losses in Ducted Flows.* Butterworth.